Supplementary Information

Polarized Mo–O Units on g-C_3N_4 for Enhanced Photo-Fenton Activity

Jun Zhao,[1,‡] Zhihao Li,[1,‡] Hongjian Deng,[2,‡] Wenjian Ma,[1] Hui Wang,[1,] Qun Zhang,[1,2,3,*] and Xiaodong Zhang,[1,*]*

[1]Hefei National Research Center for Physical Sciences at the Microscale, University of Science and Technology of China, Hefei, Anhui 230026, China

[2]Department of Chemical Physics, University of Science and Technology of China, Hefei, Anhui 230026, China

[3]Hefei National Laboratory, University of Science and Technology of China, Hefei, Anhui 230088, China

Experimental section

Synthesis of pristine CN: 2 g of dicyandiamide was placed in a 20 mL ceramic crucible, then heated at a rate of 10°C min^{-1} to 550°C and calcined for 4 hours. After natural cooling, the resulting solid product was ground into a fine powder, and labeled as CN.

Synthesis of CN-Mo-O and CN-Mo: 2 g of dicyandiamide and 0.042 g of ammonium molybdate tetrahydrate were thoroughly ground and mixed, then placed in a 20 mL ceramic crucible. The mixture was calcined at 550 °C for 4 hours in an air atmosphere, with a temperature ramp rate of 10 °C min^{-1}. After natural cooling, the resulting solid product was ground into a fine powder, and labeled as CN-Mo-O. Similarly, CN-Mo was synthesized using the same procedure, but calcined in Ar atmosphere.

Mo K-edge XAFS measurements: Mo K-edge XAFS analyses were performed with Si(111) crystal monochromators at the BL14W Beam line at the Shanghai Synchrotron Radiation Facility (SSRF) (Shanghai, China). The XAFS spectra were recorded at room temperature using a 4-channel Silicon Drift Detector (SDD) Bruker 5040. Mo K-edge extended X-ray absorption fine structure (EXAFS) spectra were recorded in transmission/fluorescence mode.

Electron spin resonance (ESR) trapping measurements:

Superoxide Radical Detection: 10 mg of the catalyst was dispersed in 1 mL of methanol and sonicated for 60 minutes to form a uniform dispersion. Then, 50 μL of this catalyst dispersion was injected into 500 μL of a methanol solution containing 2 mM 5,5-Dimethyl-1-pyrroline N-oxide (DMPO), followed by the addition of 5 μL of H_2O_2 (wt. 30%). The resulting solution was analyzed at room temperature under visible light irradiation using a Bruker EMX plus spectrometer.

Hydroxyl Radicals Detection: For the detection of hydroxyl radicals, 10 mg of catalyst was dispersed in 1 mL of deionized water and sonicated for 60 minutes to obtain a uniform dispersion. Then, 50 μL of this catalyst dispersion was injected into 500 μL of

an aqueous DMPO solution (2 mM), followed by the addition of 5 μL H_2O_2 (30 wt%). The mixture was immediately analyzed using a Bruker EMX plus spectrometer under visible light irradiation at room temperature.

Detection of Superoxide Radicals by Specific Fluorescence Probe Method: For the detection of superoxide radicals ($\cdot O_2^-$) using the specific fluorescence probe method, 2 mg of catalyst was dispersed in 10 mL of deionized water, followed by the addition of 50 μL H_2O_2 (30 wt%). The mixture was irradiated using a xenon lamp (CEL-HXF300-T3, Beijing China Education Au-light Technology Co., Ltd) equipped with a 400 nm cutoff filter as the light source. At specific illumination time intervals, the reaction solution were collected and centrifuged to obtain the supernatant. The $\cdot O_2^-$ content in the supernatant was determined using a superoxide radical assay kit (The $\cdot O_2^-$ reacts with hydroxylamine hydrochloride to produce NO_2^-, which, in the presence of sulfanilamide and N-(1-naphthyl)ethylenediamine dihydrochloride, forms a purple-red azo compound with a characteristic absorption peak at 530 nm.). The concentration of $\cdot O_2^-$ was then evaluated by measuring the absorbance in the 400-700 nm range with a UV-vis spectrophotometer.

Detection of hydroxyl radicals using terephthalic acid: 2 mg catalyst was added into 10 mL of a solution containing NaOH (10 mM) and terephthalic acid (3 mM). The mixture was stirred in the dark for 30 minutes to ensure adsorption/desorption equilibrium between the catalyst and the indicator. Subsequently, 50 μL of 30% H_2O_2 was added, and the mixture was irradiated using a xenon lamp (CEL-HXF300-T3, Beijing China Education Au-light Technology Co., Ltd.) equipped with a 400 nm cutoff filter. During the photocatalytic reaction, withdraw aliquots of the reaction solution at specific time intervals, centrifuge to obtain the supernatant, and then perform fluorescence testing and analysis.

Photo-Fenton Degradation of Methyl Orange: For the photo-Fenton degradation experiment, 2 mg of catalyst was dispersed in 10 mL of methyl orange aqueous solution

(20 mg/L), followed by the addition of 50 μL H_2O_2 (30 wt%). The mixture was irradiated using a xenon lamp (CEL-HXF300-T3, Beijing China Education Au-light Technology Co., Ltd) equipped with a 400 nm cutoff filter as the light source. At specific time intervals, 1 mL of the reaction solution were collected and centrifuged to obtain the supernatant. The degradation of methyl orange was then evaluated by monitoring the absorbance in the 300–700 nm range using a UV–visible spectrophotometer. In the sacrificial agent experiments, mannitol (0.3 g/L) and benzoquinone (0.3 g/L) were added to the reaction system as scavengers for hydroxyl radicals and superoxide radicals, respectively, while keeping all other reaction conditions unchanged.

Ultrafast spectroscopic measurements: The femtosecond time-resolved transient absorption (fs-TA) measurements were performed on a Helios pump–probe spectrometer (Ultrafast Systems LLC). The 400-nm pump pulses were delivered by an optical parametric amplifier (TOPAS-800-fs) excited by a Ti:sapphire regenerative amplifier (Coherent Legend Elite-1K-HE; center wavelength: 800 nm; pulse duration: 35 fs; pulse energy: 3 mJ; repetition rate: 1 kHz). The white-light-continuum probe pulses (440−600 nm for this work) were generated by focusing the 800 nm beam (split from the regenerative amplifier) onto a sapphire plate. The instrument response function was determined to be ~100 fs. The solution samples were contained in a 0.7-mL quartz cuvette under continuous magnetic stirring conditions, ensuring that the photoexcited volume was kept fresh during the fs-TA measurements.

Theoretical calculation method: All first-principles calculations were performed within the framework of density functional theory (DFT). The exchange-correlation energy was described using the Perdew–Burke–Ernzerhof (PBE) functional under the generalized gradient approximation (GGA). The electron-ion interactions were treated using the projector augmented-wave (PAW) method. To ensure computational accuracy, a plane-wave energy cutoff of 400 eV was set, and the "Accurate" precision level was selected to avoid aliasing or wrap-around errors. For structural optimization,

both atomic coordinates and lattice parameters were allowed to relax. Ionic relaxations were performed using the conjugate gradient (CG) algorithm (IBRION = 2). To improve the convergence of the GGA calculations, the grid density was increased (ADDGRID = .TRUE.) and non-spherical contributions were taken into account (LASPH = .TRUE.) to obtain more accurate total energies and band structures. During the calculations, the wavefunctions (LWAVE = .TRUE.) and charge densities (LCHARG = .TRUE.) were preserved for subsequent analysis. The CN-Mo model was constructed by introducing a single Mo atom into one cavity of a 2×2×1 g-C_3N_4 supercell via adsorption, utilizing the coordination-unsaturated sites of the framework. This corresponds to a Mo loading density of 25%. The CN-Mo-O model was then derived by adding an axial O ligand to the Mo center. Van der Waals interactions were treated using the DFT-D3 correction. Work function calculations were performed with dipole correction and vacuum level alignment, employing a 12 Å vacuum layer.

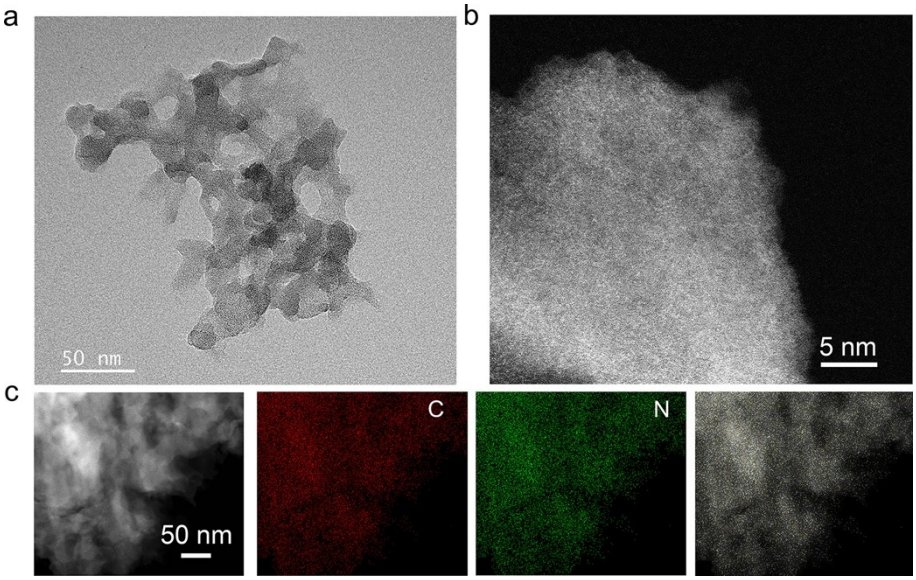

Figure S1. (a) TEM image, (b) atomic-resolution HAADF-STEM images and (c) elemental mapping images of CN.

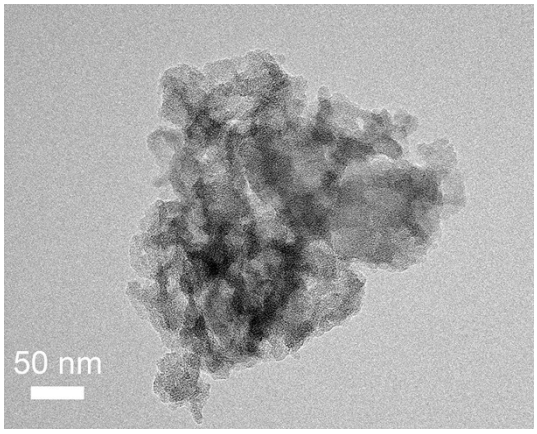

Figure S2. (a) TEM image of CN-Mo-O.

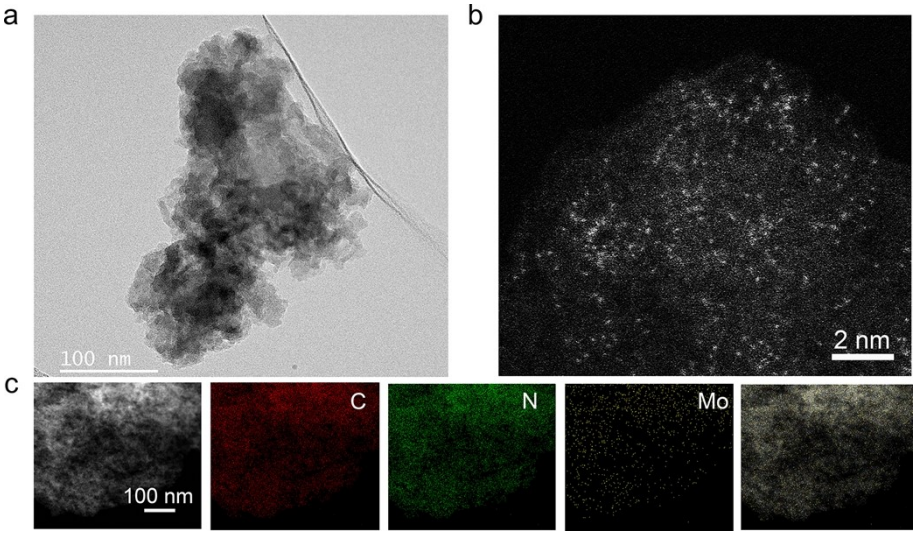

Figure S3. (a) TEM image, (b) atomic-resolution HAADF-STEM images and (c) elemental mapping images of CN-Mo.

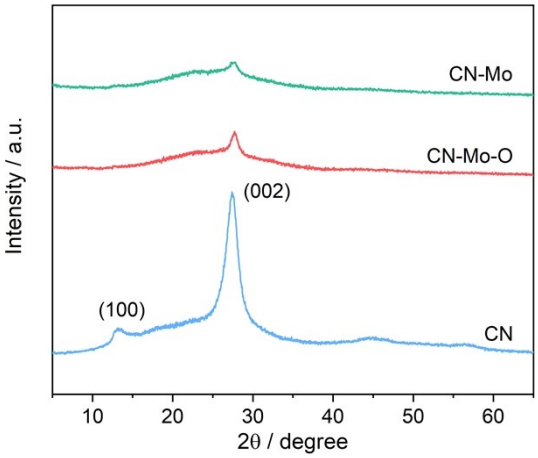

Figure S4. XRD patterns of CN, CN-Mo-O, and CN-Mo.

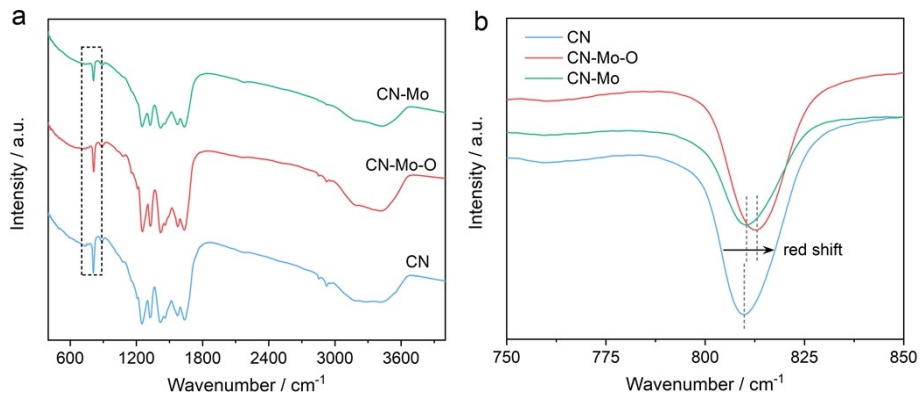

Figure S5. (a) FT-IR spectra and (b) Partial FT-IR spectra of CN, CN-Mo-O and CN-Mo.

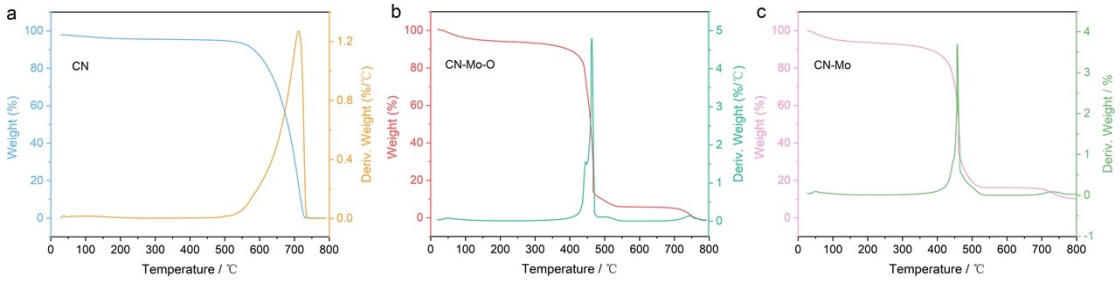

Figure S6. Thermogravimetric analyses (TGA) and differential scanning calorimetry (DSC) curves of (a) CN, (b) CN-Mo-O and (c) CN-Mo.

Thermogravimetric-differential scanning calorimetry (TG-DSC) analysis provided key insights into the thermal stability of the materials. The DSC curve of pristine CN showed a sharp exothermic peak near 700°C, corresponding to its thermal decomposition (**Fig. S6a**). In contrast, the exothermic peaks for CN-Mo and CN-Mo-O shifted significantly to around 450°C (**Fig. S6b**, **S6c**), indicating that the incorporation of Mo reduced the thermal stability of the CN framework.

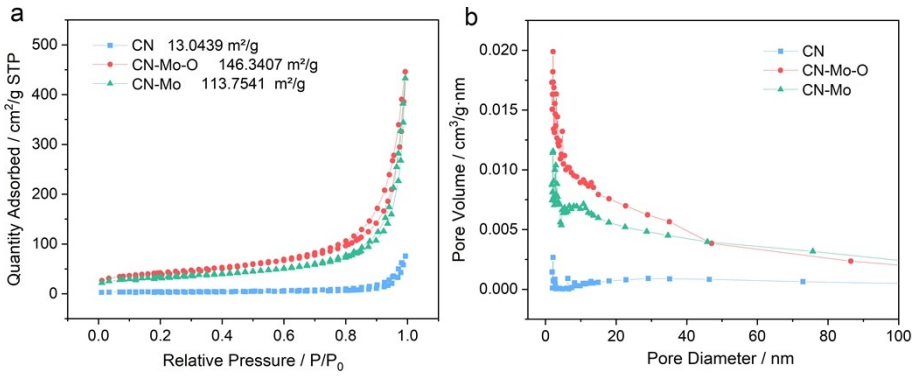

Figure S7. (a) BET and (b) pore-size distribution analyses for CN, CN-Mo-O and CN-Mo.

The BET specific surface area of the intrinsic CN, as determined from the N_2 adsorption-desorption isotherm (**Fig. S7**), was only 13 m^2/g, whereas the BET specific surface areas of CN-Mo and CN-Mo-O increased to 113.75 m^2/g and 146.34 m^2/g, respectively. Pore size distribution analysis further revealed that the CN-Mo-O sample possessed the largest pore volume. These results demonstrate that the anchoring of Mo species effectively increased the specific surface area and optimized the pore structure, which is expected to provide more active sites and facilitate mass transport during catalytic reactions.

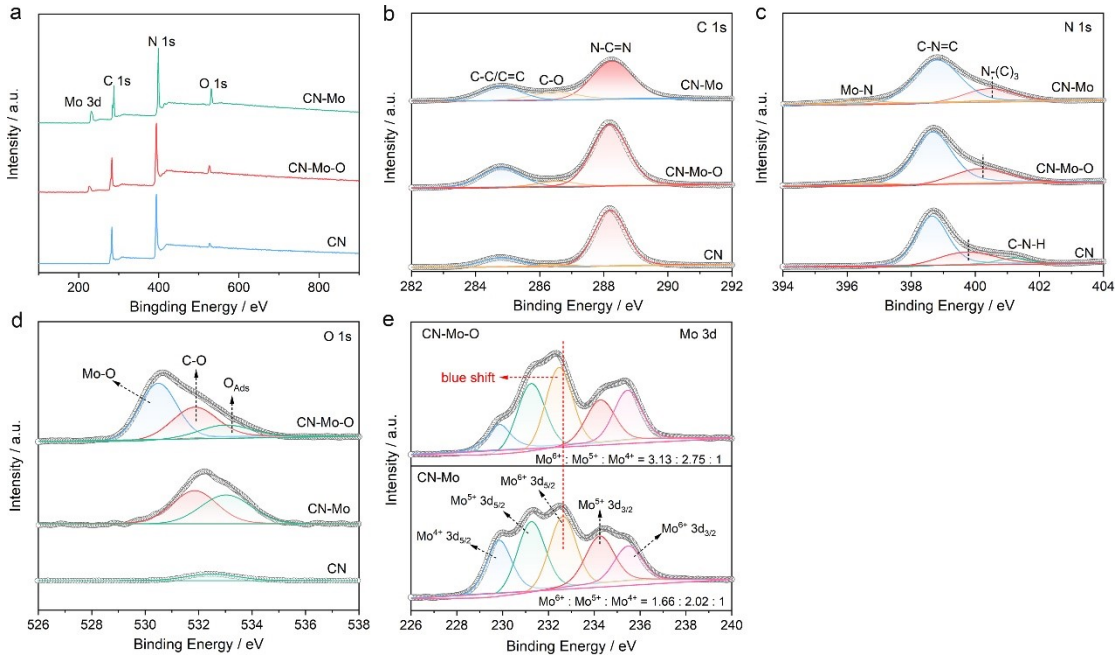

Figure S8. XPS (a) survey spectra, (b) C 1s spectra, (c) N 1s spectra and (d) O 1s spectra of CN, CN-Mo-O and CN-Mo. (e) Mo 3d spectra of CN-Mo-O and CN-Mo.

The survey spectra of CN-Mo and CN-Mo-O clearly showed characteristic Mo signals (**Fig. S8a**). The C 1s spectrum (**Fig. S8b**) decomposes into three components: the characteristic peak at 284.8 eV corresponds to C–C/C=C bonds, the peak at 286.5 eV originates from C–O bonds, and the main peak at 288.2 eV corresponds to N–C=N bonds within the CN framework.[1, 2] Compared to the CN sample, the relative content of the C–O component in CN-Mo and CN-Mo-O significantly increased, which should be attributed to the introduction of the molybdenum precursor (ammonium molybdate tetrahydrate). The N 1s spectra are shown in **Fig. S8c**. For pristine CN, the spectrum was fitted with three peaks: sp² hybridized nitrogen (C–N=C) at 398.7 eV, tertiary nitrogen (N–(C)₃) at 399.7 eV, and amino functional groups (C–N–H) at 401.3 eV.[3, 4] After Mo modification, the C–N–H peak at 401.3 eV completely disappeared in both CN-Mo and CN-Mo-O, suggesting the breakage of hydrogen-bonding network between polymer chains.[5, 6] A new peak emerged at 396.6 eV,[7, 8] providing direct evidence for the formation of Mo–N bond in the framework. In the O 1s spectra (**Fig. S8d**), the CN sample exhibits a faint peak at 532.6 eV, originating from adsorbed water or oxygen molecules on the surface.[9] For CN-Mo and CN-Mo-O, the intensity of this adsorbed

oxygen signal significantly increases, and a new peak appears at 531.9 eV, corresponding to C–O species.[10] Notably, an additional distinct peak was observed at 530.5 eV for the CN-Mo-O sample. This binding energy is characteristic of metal–oxygen bonds (M–O).[11] Analysis of the Mo 3d XPS spectra (**Fig. S8e**, **f**) provided further insight into the chemical states of Mo. The spectra were fitted with five peaks. The peaks at 235.5 eV and 234.3 eV are assigned to the Mo $3d_{3/2}$ orbitals of Mo (VI) and Mo (V), respectively. The peaks at 232.5 eV, 231.2 eV, and 229.8 eV correspond to the Mo $3d_{5/2}$ orbitals of Mo (VI), Mo (V), and Mo (IV), respectively.[12] Quantitative analysis revealed that the valence state ratio of Mo in CN-Mo was Mo (VI) : Mo (V) : Mo (IV) = 1.66 : 2.02 : 1, whereas in CN-Mo-O, the ratio was 3.13 : 2.75 : 1. This indicates that Mo exists in mixed valence states in both samples, with Mo(V) being the dominant species in CN-Mo. In contrast, CN-Mo-O exhibited a significantly higher proportion of Mo(VI), which is fully consistent with the Mo–O bond identified in its O 1s spectrum and confirms the successful introduction of higher-valence molybdenum oxide species during synthesis.

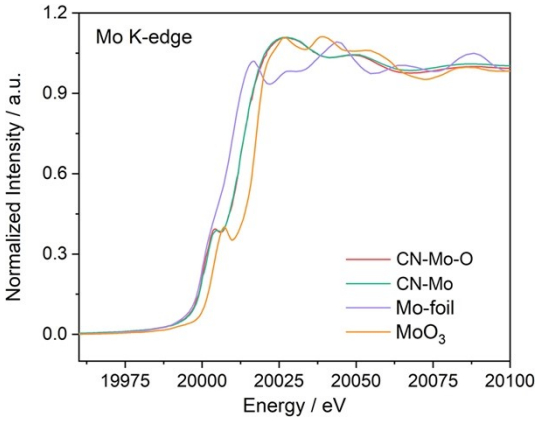

Figure S9. XANES spectra at the Mo K edge for CN-Mo-O, CN-Mo and standard Mo-foil, MoO_3.

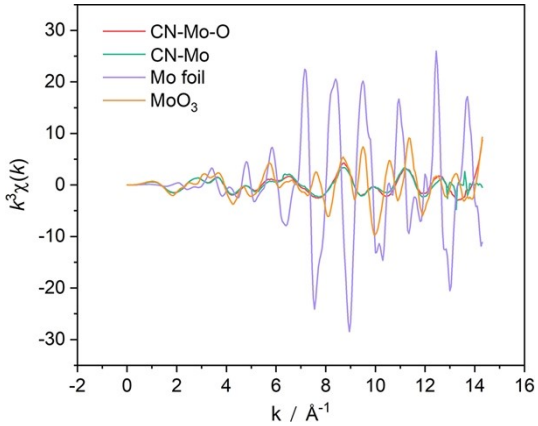

Figure S10. EXAFS spectra of CN-Mo-O, CN-Mo and standard Mo-foil, MoO_3 in k-space.

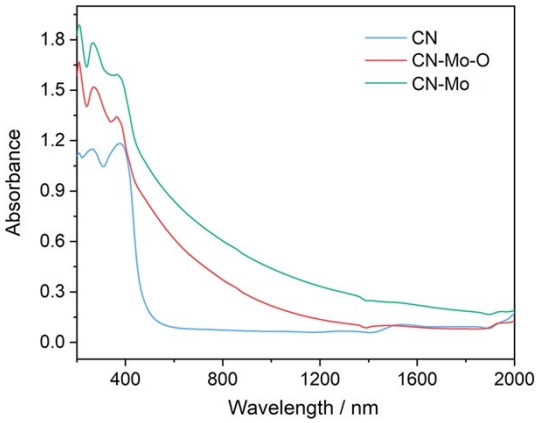

Figure S11. UV–vis spectra of CN, CN-Mo-O and CN-Mo.

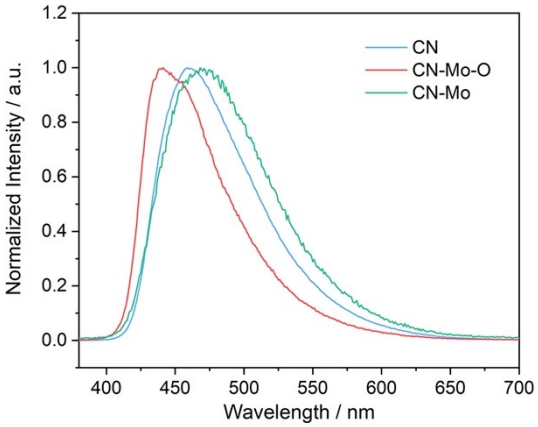

Figure S12. Normalized steady-state PL spectra of CN, CN-Mo-O and CN-Mo.

The PL emission peaks of CN-Mo and CN-Mo-O shift in opposite directions, primarily due to the different ways in which Mo species regulate the electronic structure of g-C_3N_4 under varying coordination environments. For CN-Mo, Mo species doped into the g-C_3N_4 framework introduce localized energy levels in the substrate,[13] effectively narrowing the bandgap and resulting in a redshift of the emission peak. CN-Mo-O contains Mo–O units, where the highly electronegative oxygen coordination alters the electronic structure of Mo and weakens the delocalization of the π-electron system in g-C_3N_4. This results in a slight increase in the effective bandgap of the material and therefore causing a blue shift of the luminescence peak. Similar blueshift

behavior has also been reported in g-C_3N_4 systems modified by oxygen coordination.[14-16]

Table S1. Tri-exponential fitting results of time-resolved PL spectra of CN, CN-Mo-O and CN-Mo.

Materials	CN	CN-Mo-O	CN-Mo
T1 / ns	2.41 ± 0.12 (48.7%)	2.75 ± 0.14 (48.5%)	2.28 ± 0.10 (45.3%)
T2 / ns	10.48 ± 0.28 (31.7%)	10.67 ± 0.26 (35.2%)	11.43 ± 0.29 (32.5%)
T3 / ns	0.52 ± 0.03 (19.6%)	0.64 ± 0.02 (16.3%)	0.40 ± 0.01 (22.2%)
Average LifeTime / ns	1.65 ± 0.30	2.16 ± 0.30	1.27 ± 0.31

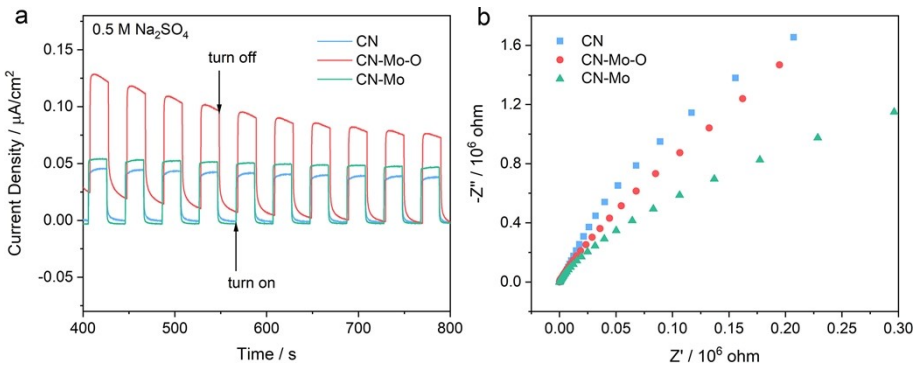

Figure S13. (a) Periodic on/off photocurrent responses and (b) EIS of CN, CN-Mo-O and CN-Mo.

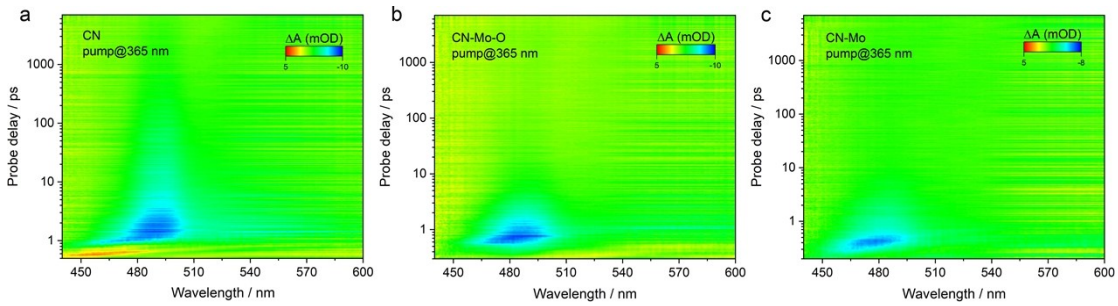

Figure S14. Contour maps of fs-TA of (a) CN, (b) CN-Mo-O, and (c) CN-Mo, excited at 365 nm and probed in the wavelength range of 440–600 nm.

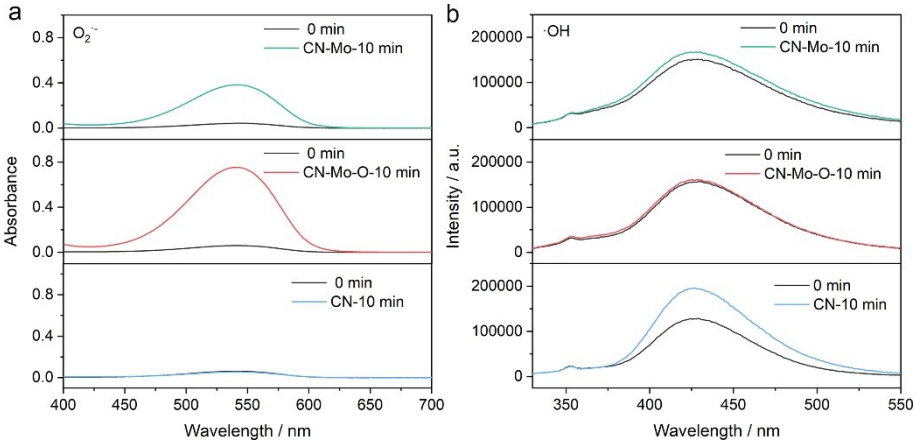

Figure S15. (a) Detection of $\bullet O_2^-$ generated from photo-Fenton reaction using a commercial assay kit. (b) Detection of •OH generated in the photo-Fenton reaction by terephthalic acid.

In addition to EPR characterization, we performed quantitative analysis of reactive oxygen species generation in different systems using molecular probe experiments. Using a commercial superoxide radical detection kit (**Fig. S15a**), we found that after 10 minutes of illumination, the CN–H_2O_2 system produced almost no $\bullet O_2^-$, while the CN-Mo-O–H_2O_2 system generated the highest amount of $\bullet O_2^-$, followed by the CN-Mo–H_2O_2 system. Meanwhile, experiments using terephthalic acid as an •OH probe

(**Fig. S15b**) showed that under the same conditions, after 10 minutes of illumination, the CN–H_2O_2 system produced the highest amount of •OH, the CN-Mo–H_2O_2 system generated only trace amounts of •OH, and the CN-Mo-O–H_2O_2 system produced almost no •OH. These results are fully consistent with the EPR data, collectively confirming that CN-Mo-O can efficiently and selectively generate $•O_2^-$.

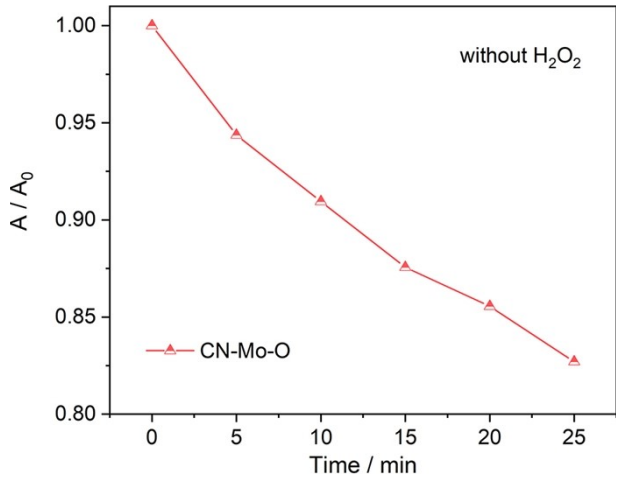

Figure S16. Photocatalytic degradation of methyl orange by CN-Mo-O (catalyst dosage = 0.2 mg·mL^{-1}; [Methyl Orange] = 20 mg·L^{-1}).

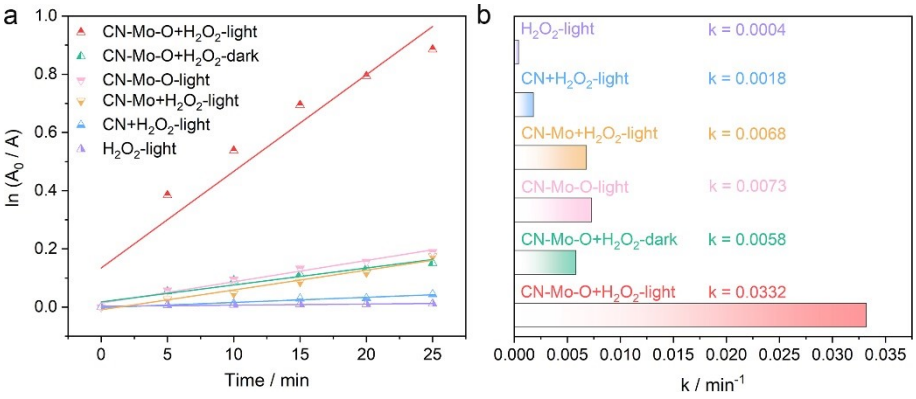

Figure S17. The apparent rate constants (k) of the first-order kinetics for different photo-Fenton catalytic systems.

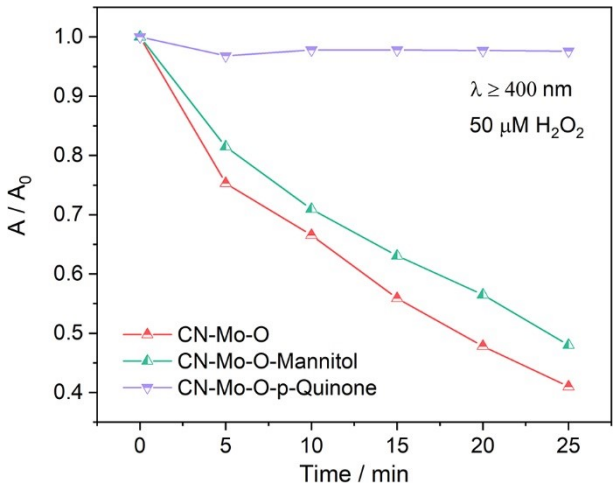

Figure S18. Methyl orange degradations of the CN-Mo-O photo-Fenton system in the absence/presence of different scavengers.

To further quantify the contributions of different reactive oxygen species in methyl orange degradation, we have supplemented scavenger experiments. In the CN-Mo-O photo-Fenton system for methyl orange degradation, mannitol (0.3 mg/mL, a •OH scavenger) and p-quinone (0.3 mg/mL, an $O_2^{\bullet-}$ scavenger) were separately introduced. As shown in **Fig. S18**, the degradation efficiency of methyl orange was not significantly affected after adding mannitol, whereas almost no degradation occurred after adding p-quinone. These scavenger experiments clearly demonstrates that methyl orange degradation in this system is predominantly driven by $O_2^{\bullet-}$, which further confirms the selective $O_2^{\bullet-}$-generation capability in the CN-Mo-O–H_2O_2 system.

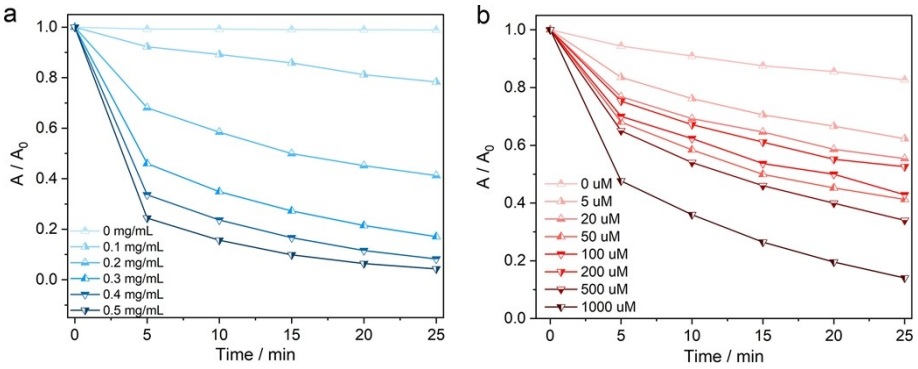

Figure S19. Effects of (a) catalyst dosage and (b) H_2O_2 dosage on CN-Mo-O-based photo-Fenton catalytic degradation of methyl orange.

We further optimized the reaction conditions for the CN-Mo-O system. As shown in **Fig. S19a**, the methyl orange degradation efficiency increased with catalyst dosage (0–0.5 mg mL^{-1}), showing significant enhancement up to 0.3 mg mL^{-1} before leveling off, indicating full utilization of active sites at higher loadings. The effect of H_2O_2 concentration was not simply positive (**Fig. S19b**). When the concentration increased from 50 mM to 200 mM, the degradation efficiency decreased, may be related to the reaction between H_2O_2 and the radicals.

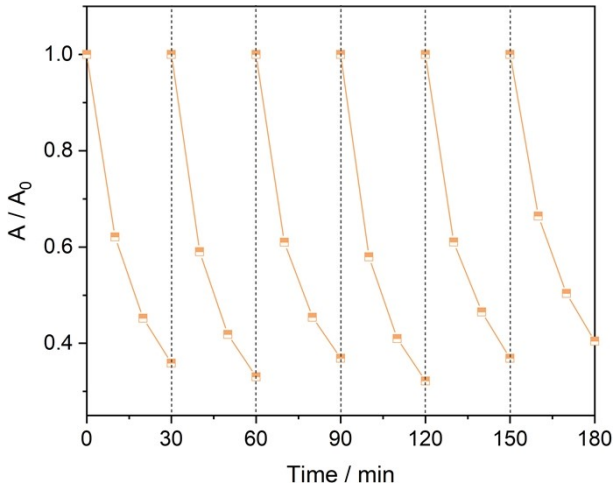

Figure S20. The cycling tests of CN-Mo-O-based photo-Fenton catalytic degradation of methyl orange.

In addition, cyclic stability testing was conducted through continuous repeated photocatalytic Fenton-degradation experiments. Each cycle was conducted for 30 min, followed by recovery of the catalyst, which was then washed, dried, and reused in the subsequent cycle. The catalyst retained stable activity after six consecutive recycling tests (**Fig. S20**), confirming its good reusability.

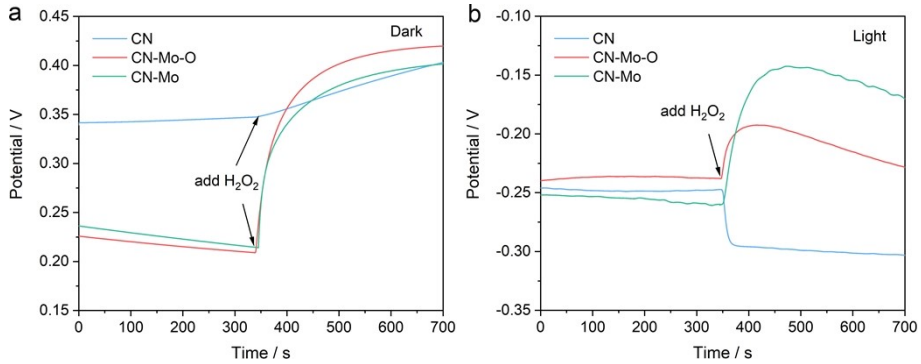

Figure S21. Open-circuit potential of CN, CN-Mo-O, and CN-Mo under (a) dark and (b) light conditions. An injection of 200 μL H_2O_2 (1 M) was introduced at 350 s.

To further investigate the charge transfer between the catalysts and H_2O_2, open-circuit potential (OCP) measurements were performed under both dark and illuminated conditions. In the dark (**Fig. S21a**), the addition of H_2O_2 caused a positive shift in the OCP for all samples, primarily attributed to the chemisorption of H_2O_2. Among them, CN-Mo-O showed the most pronounced shift, indicating its strongest adsorption affinity for H_2O_2. Under illumination **(Fig. S21b**), the OCP of pristine CN shifted negatively after H_2O_2 addition. Based on the EPR data, this phenomenon can be attributed to electron accumulation resulting from hole consumption. This result aligns with the EPR results that ·OH is the main ROS in the CN system, generated mainly through hole-induced oxidation of H_2O_2. In contrast, the OCP curves of CN-Mo and CN-Mo-O exhibited an initial rapid positive shift followed by a gradual negative drift. Notably, the amplitude of the initial positive shift under illumination was significantly smaller compared to that in the dark. This attenuation indicates a transition from a mere adsorption-dominated process to a rapid catalytic cycle involving continuous adsorption and in-situ reaction of H_2O_2 at the Mo active sites. Furthermore, CN-Mo-O showed the smallest positive shift amplitude, demonstrating its highest catalytic activity. This implies that in CN-Mo-O, photogenerated electrons are consumed at the fastest rate via the most efficient electron transfer pathway, enabling the most rapid H_2O_2 activation kinetics.

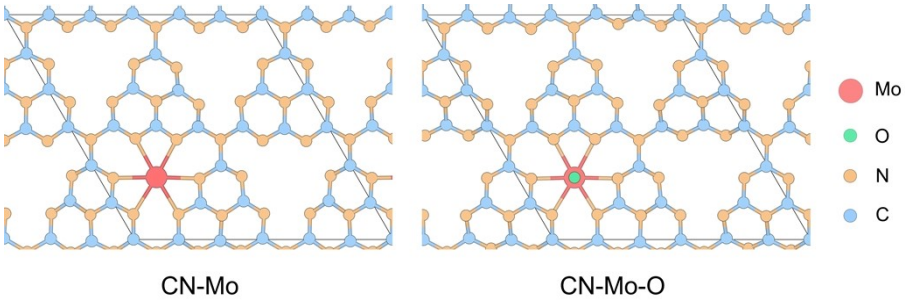

Figure S22. Theoretical models of CN-Mo and CN-Mo-O.

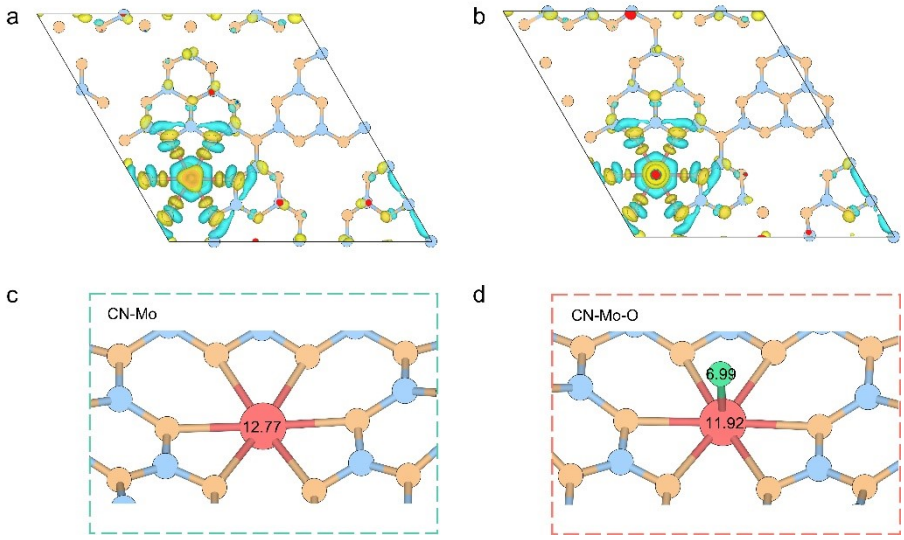

Figure S23. Differential charge density maps of (a) CN-Mo and (b) CN-Mo-O. Bader charges of (c) CN-Mo and (d) CN-Mo-O.

Reference

1. J. Cao, C. Qin, Y. Wang, H. Zhang, B. Zhang, Y. Gong, X. Wang, G. Sun, H. Bala and Z. Zhang, *RSC Adv.*, 2017, **7**, 25504-25511.
2. S.-W. Cao, Y.-P. Yuan, J. Barber, S. C. J. Loo and C. Xue, *Appl. Surf. Sci.*, 2014, **319**, 344-349.
3. X. Li, W. Bi, L. Zhang, S. Tao, W. Chu, Q. Zhang, Y. Luo, C. Wu and Y. Xie, *Adv. Mater.*, 2016, **28**, 2427-2431.
4. J. Han, X. Ji, X. Ren, G. Cui, L. Li, F. Xie, H. Wang, B. Li and X. Sun, *J. Mater. Chem. A*, 2018, **6**, 12974-12977.
5. X. Chen, L. Zhang, B. Zhang, X. Guo and X. Mu, *Sci. Rep.*, 2016, **6**, 28558.
6. F. He, G. Chen, Y. Yu, S. Hao, Y. Zhou and Y. Zheng, *ACS Appl. Mater. Interfaces*, 2014, **6**, 7171-7179.
7. R. Zhang, P. Li, F. Wang, L. Ye, A. Gaur, Z. Huang, Z. Zhao, Y. Bai and Y. Zhou, *App. Catal. B: Environ.*, 2019, **250**, 273-279.
8. P. Du, K. Hu, J. Lyu, H. Li, X. Lin, G. Xie, X. Liu, Y. Ito and H.-J. Qiu, *App. Catal. B: Environ.*, 2020, **276**, 119172.
9. H. Idriss, *Surf. Sci.*, 2021, **712**, 121894.
10. J. Zhao, H. Li, Z. Li, S. Jiang, M. Guan, P. Zhang, S. Shang, Z. Zhao, H. Wang, Q. Zhang, X. Zhang and Y. Xie, *Natl. Sci. Rev.*, 2025, **12**, nwaf062.
11. C. Ye, H. Cheng, L. Zheng, J. Lin, Q. Xu, Y. Qiu, Z. Pan and Y. Qiu, *Nano Lett.*, 2023, **23**, 1573-1581.
12. J. G. Choi and L. T. Thompson, *Appl. Surf. Sci.*, 1996, **93**, 143-149.
13. Y. Li, Z. Wang, T. Xia, H. Ju, K. Zhang, R. Long, Q. Xu, C. Wang, L. Song, J. Zhu, J. Jiang and Y. Xiong, *Adv. Mater.*, 2016, **28**, 6959-6965.
14. H. Wang, S. Jiang, S. Chen, D. Li, X. Zhang, W. Shao, X. Sun, J. Xie, Z. Zhao, Q. Zhang, Y. Tian and Y. Xie, *Adv. Mater.*, 2016, **28**, 6940-6945.
15. Q. Li, Y. Jiao, Y. Tang, J. Zhou, B. Wu, B. Jiang and H. Fu, *J. Am. Chem. Soc.*, 2023, **145**, 20837-20848.
16. J. Hou, K. Wang, X. Zhang, Y. Wang, H. Su, C. Yang, X. Zhou, W. Liu, H. Hu, J. Wang, C. Li, P. Ma, R. Zhang, Z. Wei, Z. Sun, Q. Liu and K. Zheng, *ACS Catal.*, 2024, **14**, 10893-10903.